



**MoS<sub>2</sub>-Capped Cu<sub>x</sub>S Nanocrystals: A New Heterostructured  
Geometry of Transition Metal Dichalcogenides for  
Broadband Optoelectronics**

Journal:	<i>Materials Horizons</i>
Manuscript ID	MH-COM-07-2018-000809.R1
Article Type:	Communication
Date Submitted by the Author:	19-Sep-2018
Complete List of Authors:	<p>Li, Yuan; Northwestern University, Materials Science and Engineering  Murthy, Akshay; Northwestern University, Materials Science and Engineering  Distefano, Jennifer; Northwestern University, Materials Science and Engineering  Jung, Hee Joon; Northwestern University, Department of Materials Science and Engineering; Northwestern University, International Institute for Nanotechnology; Northwestern University, Northwestern University Atomic and Nanoscale Characterization Experimental (NUANCE) Center  Hao, Shiqiang; Northwestern University, Materials Science  Villa, Cesar ; Northwestern University, Materials Science and Engineering  Wolverton, Chris; Northwestern University, Department of Materials Science and Engineering  Chen, Xinqi; Northwestern University, Materials Science and Engineering  David, Vinayak; Northwestern University, Materials Science &amp; Engineering</p>

### **Conceptual Insight Statement**

The conventional TMD heterostructures, aligned in lateral or vertical geometries (e.g., MoS<sub>2</sub>/WS<sub>2</sub>, MoSe<sub>2</sub>/WSe<sub>2</sub>, WSe<sub>2</sub>/MoS<sub>2</sub>, etc.), exhibit new chemical, structural and electronic properties for various applications in transistors, diodes and photovoltaic/photodetection devices. However, the main protocols, mechanical transfer and chemical vapor deposition, for preparing such heterostructures, are limited for their inevitable interface contamination and lack of massive and constant yield. Beyond the scope of such traditional heterostructures, our study reports a critical scientific step forward for bringing the concept of a new heterostructural geometry (namely MoS<sub>2</sub>-capped Cu<sub>x</sub>S nanocrystals) into the family of TMD heterostructures. By using a direct chemical vapor deposition approach, we are able to create an atomically clean interface between Cu<sub>x</sub>S core and MoS<sub>2</sub> cap, which, as compared with the conventional TMD heterostructures, effectively maximized the interfacial area and would be very facile to realize the large-scale production. Our structural design and synthesis strategy of the MoS<sub>2</sub>-capped Cu<sub>x</sub>S nanocrystals can be generalized to abundant of TMD materials and thus allow for wide range of exploration across diverse disciplines and originality of the approach.

# MoS<sub>2</sub>-Capped Cu<sub>x</sub>S Nanocrystals: A New Heterostructured Geometry of Transition Metal Dichalcogenides for Broadband Optoelectronics

*Yuan Li,<sup>a,b</sup> Akshay A. Murthy,<sup>a,d</sup> Jennifer G. DiStefano,<sup>a</sup> Hee Joon Jung,<sup>a,b</sup> Shiqiang Hao,<sup>a</sup> Cesar J. Villa,<sup>a</sup> Chris Wolverton,<sup>a</sup> Xinqi Chen,<sup>b,c,\*</sup> Vinayak P. Dravid<sup>a,b,d,\*</sup>*

<sup>a</sup> Department of Materials Science and Engineering, <sup>b</sup> Northwestern University Atomic and Nanoscale Characterization Experimental (NUANCE) Center, <sup>c</sup> Department of Mechanical Engineering, and <sup>d</sup> International Institute for Nanotechnology (IIN), Northwestern University, Evanston, Illinois 60208, USA

\*Corresponding author

Xinqi Chen: [x-chen@northwestern.edu](mailto:x-chen@northwestern.edu)

Vinayak P. Dravid: [v-dravid@northwestern.edu](mailto:v-dravid@northwestern.edu)

\*\*\*\*\*

†Electronic supplementary information (ESI†) available: Experimental details; XRD characterization; Transfer of CVD-grown MoS<sub>2</sub> monolayer onto Cu<sub>x</sub>S nanocrystals.

**Abstract**

Heterostructuring of different transition metal dichalcogenides (TMDs) leads to interesting band alignment and performance improvement, and thus enables new routes of materials development for next-generation semiconductor electronics. Herein, we introduce a new strategy for the design and synthesis of functional TMD heterostructures. The representative product, molybdenum disulfide-capped copper sulfide ( $\text{Cu}_x\text{S}@MoS_2$ ,  $1.8 < x < 2.0$ ), is typically obtained by chemical vapor deposition of cap-like  $MoS_2$  layers on  $Cu_xS$  nanocrystals, yielding the formation of a sharp, clean heterojunction interface. The heterostructures exhibit strong light-matter interactions over a broadband range, with interesting band alignment for separating photocarriers and mediating charge transfer. A phototransistor made from  $Cu_xS@MoS_2$  heterostructures shows particularly high photoresponse for near infrared light, which is enabled by the heterojunction of  $MoS_2$  with a small band gap semiconductor as well as the plasmonic enhancement from  $Cu_xS$  nanocrystals. Our study paves a way for the development of new TMD heterostructures towards achieving functional electronics and optoelectronics.

**Keywords:**  $MoS_2$ ;  $Cu_xS$ ; heterostructure; light-matter interaction, optoelectronics

## 1. Introduction

Semiconductor heterostructures are essential components in modern high-speed electronics and optoelectronic devices.<sup>1</sup> With the need for continued device scaling to achieve faster and miniaturized electronic components, new semiconductor systems, such as the two-dimensional (2D) transition metal dichalcogenides (TMDs) have attracted broad interest due to their unique layer-dependent electronic and optical properties.<sup>2-4</sup> When these TMD semiconductors are combined in tandem, exciting new chemical, structural and electronic properties for various applications, such as transistors, diodes and photovoltaic/photodetection devices, are observed.<sup>5-10</sup> For instance, heterostructures of layered TMDs (e.g., MoS<sub>2</sub>/WS<sub>2</sub>,<sup>7</sup> MoSe<sub>2</sub>/WSe<sub>2</sub>,<sup>8</sup> WSe<sub>2</sub>/MoS<sub>2</sub>,<sup>9,10</sup> etc.) have been demonstrated to form p-n junctions, which serve as the basis for these optoelectronic devices. The main function of these heterostructures is the ability to mediate optical transitions and charge transfer across the junction of two materials,<sup>11-13</sup> and thus, maintaining a large-area, clean, and high-quality interface is of great importance. Unfortunately, to date most reported 2D heterostructures have been fabricated through mechanical transfer methods or multi-step chemical vapor deposition. While the former is troublesome due to the interfacial contamination commonly introduced *via* the polymer-based transfer process, the latter is problematic due to challenges related to a lack of spatial control over the synthesized products, a more limited heterojunction interface, and a lack of consistent yield.<sup>7</sup>

Toward this end, exploring new geometries of TMDs heterostructures beyond the existing library of 2D materials is of great interest for interface engineering and scalable production. Recently, surface decoration of TMD monolayers with nanocrystals<sup>14-16</sup> or quantum dots<sup>17,18</sup> of other chalcogenides has been studied as a typical approach to create heterojunctions. The resultant nanocomposites can effectively overcome the low optical cross-section of MoS<sub>2</sub> and thus led to

enhanced absorption<sup>14</sup> and improved photodetectivity<sup>18</sup>. For instance, chalcocite copper sulfide ( $\text{Cu}_x\text{S}$ ) nanocrystals are one of the most interesting materials due to their natural abundance, p-type semiconductor nature, and relatively small band gap leading to strong light absorption from visible to near infrared region.<sup>19,20</sup> When combined with  $\text{MoS}_2$ , the resultant band alignment at the interfaces can potentially enable the superior interfacial charge transfer.<sup>21,22</sup> However, the reported preparation of these TMD heterostructures mostly relies on mechanical transfer<sup>14,15</sup> or solution-based chemical synthesis<sup>16,17</sup> and thus has been difficult to realize an uncontaminated and atomically-contacted sharp interface.

Herein we introduce a new geometry design for the family of TMD heterostructures by encapsulating  $\text{Cu}_x\text{S}$  ( $1.8 < x < 2$ ) nanocrystals with cap-like  $\text{MoS}_2$  layered structures, namely  $\text{Cu}_x\text{S}@MoS_2$  heterostructures. An atomically clean interface between  $\text{Cu}_x\text{S}$  core and  $\text{MoS}_2$  cap is created *via* direct chemical vapor deposition, which effectively maximizes the interfacial area and thus facilitates photoemission and charge transfer between the two materials. Using discrete dipole approximation (DDA), we examined the optical properties of these heterostructures and density functional theory (DFT) calculations were conducted to better understand the band alignment and charge transfer dynamics at the heterojunction interface. The viability of the heterostructures for photodetection applications was evaluated as well. The results indicate that our  $\text{Cu}_x\text{S}@MoS_2$  heterostructures exhibit highly improved light-matter interactions over a broad wavelength range compared to bare  $\text{MoS}_2$ , and thus lead to a strong photoresponse from violet to near-infrared light.

## 2. Results and discussion

The synthesis of  $\text{Cu}_x\text{S}@MoS_2$  heterostructures is illustrated in Fig. 1a. Briefly, a 4-nm Cu film was first deposited on a Si/SiO<sub>2</sub> substrate by thermal evaporation and then annealed at 600 °C in N<sub>2</sub> environment (step 1). The samples were then sulfurized at 600 °C (step 2) for 30 min. The encapsulation of MoS<sub>2</sub> caps was finally accomplished *via* a chemical vapor deposition process utilizing MoO<sub>3</sub> and S powders as precursors (step 3). The resultant product,  $\text{Cu}_x\text{S}@MoS_2$  heterostructure, is schematically illustrated in Fig. 1b. An optical image of the resultant sample surface is shown in Fig. 1c. The Cu film within the dotted lines was removed by scratching prior to the MoS<sub>2</sub> deposition. Thus, in this region, which exhibits a lighter optical contrast, we observed the growth of MoS<sub>2</sub> monolayers with no  $\text{Cu}_x\text{S}$ . The flakes outside the dotted region exhibit relatively darker color due to the formation of  $\text{Cu}_x\text{S}@MoS_2$  heterostructures, as indicated by the SEM images in Fig. 1d and e. One can also observe that the  $\text{Cu}_x\text{S}@MoS_2$  nanocrystals are distributed uniformly throughout the substrate. It is worth noting that the size and distribution of the nanocrystals can be effectively modulated by varying the thickness of preliminary Cu film and the ramp rate of the subsequent annealing process, similar to that we have otherwise demonstrated previously.<sup>23</sup> XRD patterns obtained over the entire substrate (Fig. S1, ESI†) indicate that the  $\text{Cu}_x\text{S}$  nanocrystals have a chalcocite structure with  $x$  varying from 1.8 to 2.0.

TEM images in Fig. 1f and g confirm that the MoS<sub>2</sub> layers, with a layer-to-layer spacing of 6.6 Å and thickness of ~3-5 nm, are capped on the faceted  $\text{Cu}_x\text{S}$  nanocrystals. The high-resolution image (Fig. 1h) further indicates the direct atomic connection of  $\text{Cu}_x\text{S}$  and MoS<sub>2</sub> at the interface. The  $\text{Cu}_x\text{S}$  exhibits a lattice spacing of 3.1 Å, corresponding to the (200) plane, which is also found to be the dominant facet of  $\text{Cu}_x\text{S}$  from the diffraction pattern (Fig. 1i). EDS maps conducted on a typical  $\text{Cu}_x\text{S}@MoS_2$  heterostructure (Fig. 1j), demonstrate the elemental

composition of Cu, Mo and S (Fig. 1k-m). The distribution of Cu is mostly concentrated inside the heterostructure as outlined in Fig. 1j, indicating effective MoS<sub>2</sub> encapsulation of the Cu<sub>x</sub>S nanocrystals.

XPS demonstration is further displayed in Fig. 2a-c. The spectra for the Cu<sub>x</sub>S@MoS<sub>2</sub> heterostructures are compared to a control sample prepared by transferring a pre-grown MoS<sub>2</sub> monolayer onto Cu<sub>x</sub>S nanocrystals (represented as Cu<sub>x</sub>S/MoS<sub>2</sub> hereafter). Details about the MoS<sub>2</sub> transfer can be found in Fig. S2 (ESI†). The Mo and S spectra are generally consistent for both samples. The Mo 3d peaks at 233.11 eV and 229.92 eV correspond to the 3d<sub>5/2</sub> and 3d<sub>3/2</sub> doublets (Fig. 2a); while the S 2p peak can be deconvoluted into two peaks at 163.91 eV and 162.73 eV (Fig. 2b), which can be assigned to the 2p<sub>1/2</sub> and 2p<sub>3/2</sub> orbitals, respectively.<sup>24,25</sup> The peaks for metallic Mo or MoO<sub>x</sub> are insignificant, suggesting high quality MoS<sub>2</sub> layers on both products. The Cu<sub>x</sub>S@MoS<sub>2</sub> heterostructures present Cu 2p peaks at 952.32 eV (2p<sub>1/2</sub>) and 932.45 eV (2p<sub>3/2</sub>), which are consistent with the peak location of copper sulfides.<sup>26</sup> However, the intensity of Cu peaks is weaker compared with the Mo and S peaks, due to the encapsulation of MoS<sub>2</sub> layers. It is worth noting that peaks representing CuSO<sub>4</sub> are also observed on the transferred samples, probably due to the inevitable surface oxidation of Cu<sub>x</sub>S in air, which indicates that MoS<sub>2</sub> encapsulation leads to improved air stability of the nanocrystals and serves as an additional highlight of this geometry.

Raman spectroscopy is used to assess the crystallinity and layer thickness of MoS<sub>2</sub> layers through the two characteristic MoS<sub>2</sub> vibrational modes,  $E_{2g}^1$  and  $A_{1g}$ .<sup>25,27</sup> The  $E_{2g}^1$  mode is attributed to the in-plane vibration of Mo and S atoms, while the  $A_{1g}$  mode is related to the out-of-plane vibration of S atoms.<sup>27</sup> Fig. 2d shows the Raman spectra of monolayer MoS<sub>2</sub> (spectrum 1,



obtained inside the dotted lines in Fig. 1b),  $\text{Cu}_x\text{S}/\text{MoS}_2$  (spectrum 2) and  $\text{Cu}_x\text{S}@/\text{MoS}_2$  (spectrum 3). The  $\text{Cu}_x\text{S}@/\text{MoS}_2$  heterostructures exhibit the two vibrational modes centered at  $381.10\text{ cm}^{-1}$  and  $403.23\text{ cm}^{-1}$  with a  $E_{2g}^1$ -to- $A_{1g}$  frequency difference of  $\sim 22.13\text{ cm}^{-1}$ . This value is smaller than that of bulk  $\text{MoS}_2$ , but larger than that of the pristine and transferred monolayer  $\text{MoS}_2$ , probably due to the multilayer nature of the  $\text{MoS}_2$  caps.<sup>28</sup> Corresponding photoluminescence spectra are also collected at ambient temperature with a small laser power of  $1\text{ }\mu\text{W}$  to avoid heating the sample. As shown in Fig. 2e, the pristine  $\text{MoS}_2$  exhibits photoluminescence emission near  $\sim 674\text{ nm}$  and another insignificant emission peak around  $\sim 623\text{ nm}$ . The former is attributed to A exciton emission from the interband transition at the Brillouin zone K point in  $\text{MoS}_2$ , while the latter arises from the higher energy B exciton emission from another direct transition between the conduction band and a lower-lying valence band.<sup>29,30</sup> The  $\text{Cu}_x\text{S}@/\text{MoS}_2$  heterostructures exhibit equivalent photoluminescence emission peaks, with a slight blue-shift ( $670\text{ nm}$ ) probably originated from the change of local strain because of the presence of  $\text{Cu}_x\text{S}$  cores.<sup>31</sup> It is worth noting that a remarkable quenching effect and more significant blue-shift (to  $663\text{ nm}$ ) of the photoluminescence was observed for the transferred  $\text{MoS}_2$  sample, probably due to the inevitable contamination and released local strain from the original  $\text{SiO}_2$  substrate after the transfer process.<sup>32</sup> This again proves the necessity of building a clean interface as demonstrated in our heterostructures.

The optical properties of the  $\text{Cu}_x\text{S}@/\text{MoS}_2$  heterostructures are further understood using discrete dipole approximation (DDA) method. The simulation was carried out for a  $50 \times 25 \times 25\text{ nm}^3$  rectangular  $\text{Cu}_x\text{S}$  target and the same  $\text{Cu}_x\text{S}$  capped with 6-layer  $\text{MoS}_2$  as shown in Fig. 3a and b, respectively. The details regarding the DDA method can be found in the experimental section (ESI†).<sup>33,34</sup> The simulated absorption spectra are shown in Fig. 3c. The  $\text{Cu}_x\text{S}$  nanocrystal shows high absorption in the visible region ( $400\text{ nm}$  to  $600\text{ nm}$ ) as well as the near infrared region ( $700$

nm to 1000 nm), which is consistent with previous experimental report.<sup>35</sup> The  $\text{Cu}_x\text{S}@\text{MoS}_2$  heterostructure exhibits overall increased absorption in the visible region, with the emergence of two peaks at 673.1 nm and at 628.0 nm due to the presence of A and B exciton absorption pathways indicated in Fig. 3e.

The DDA calculations also model the interaction of refractive index with geometry and incident light to evaluate electric field distribution,<sup>33</sup> which is an indicator of the magnitude of light-matter interaction present. Fig. 3d-i display the front view (arrow direction in Fig. 3a) of the obtained electric field maps of both targets at different incident wavelengths (400 nm, 610 nm and 900 nm). The electric field strength ( $|E/E_0|^2$ ) can be correlated to the absorption efficiency at various locations of the sample in Fig. 3c. Overall, one can observe that the  $\text{Cu}_x\text{S}$  nanocrystal shows a weak electric field response (Fig. 3d-f), while the electric field distribution of the  $\text{Cu}_x\text{S}@\text{MoS}_2$  heterostructure is confined in the  $\text{MoS}_2$  cap, with significantly enhanced strength (Fig. 3g-i), suggesting the significant improvement of light-matter interactions due to the formation of a heterojunction. This aspect is particularly clear under an incident radiation of 900 nm, where even though coupling of light with the localized surface plasmon resonance (LSPR) of  $\text{Cu}_x\text{S}$  leads to an enhanced electric field in the bare nanocrystal.<sup>36,37</sup> By contrast, the  $\text{Cu}_x\text{S}@\text{MoS}_2$  heterostructure exhibits a stronger response, due to the possible plasmonic coupling enabled by the clean  $\text{Cu}_x\text{S}$ - $\text{MoS}_2$  interface.<sup>31</sup> These simulations suggest that our  $\text{Cu}_x\text{S}@\text{MoS}_2$  heterostructure is a promising optoelectronic material particularly for applications where near infrared source is required.

The DDA results theoretically suggest interesting light-matter interactions in our  $\text{Cu}_x\text{S}@\text{MoS}_2$  heterostructures, allowing us to further explore their potential application in broadband optoelectronics. A field-effect phototransistor made from the  $\text{Cu}_x\text{S}@\text{MoS}_2$

heterostructures were constructed with a schematic provided in Fig. 4a. In this device geometry,  $\text{Cu}_x\text{S}@\text{MoS}_2$  heterostructures act as the light sensitizers, while the underlying  $\text{MoS}_2$  monolayers act as the channel material (Fig. 4b). A similar transistor made from the transferred  $\text{Cu}_x\text{S}/\text{MoS}_2$  is also studied for comparison. All measurements were conducted at room temperature. As shown in Fig. 4c, the transferred  $\text{Cu}_x\text{S}/\text{MoS}_2$  device exhibits a typical n-type channel behavior, which is consistent with the n-type nature of monolayer  $\text{MoS}_2$ .<sup>30</sup> The  $\text{Cu}_x\text{S}@\text{MoS}_2$  device also shows a n-type electronic behavior, however a gate-dependent drain current was only observed for small positive gate voltages before immediately saturating. This is possibly due to the Fermi level of  $\text{MoS}_2$  being aligned with that of p-type  $\text{Cu}_x\text{S}$  after the formation of heterojunction. Further increase of gate voltage at the positive direction can lead to misalignment in these bands, which would induce a decrease in the current.<sup>38</sup> From the transfer curves, we obtain a carrier mobility of  $1.76 \times 10^{-4} \text{ cm}^2 \text{ V}^{-1} \text{ s}^{-1}$  for the  $\text{Cu}_x\text{S}@\text{MoS}_2$  device and  $0.11 \times 10^{-4} \text{ cm}^2 \text{ V}^{-1} \text{ s}^{-1}$  for the  $\text{Cu}_x\text{S}/\text{MoS}_2$  device. It is also worth noting that both devices show a relatively weak gate dependence with ON/OFF ratio of 1.2~1.5,<sup>39</sup> which is probably due to the electric field screening provided by the underlying  $\text{Cu}_x\text{S}$  nanocrystals. The dependence of transfer curves on the illumination power for the  $\text{Cu}_x\text{S}/\text{MoS}_2$  and  $\text{Cu}_x\text{S}@\text{MoS}_2$  transistors is demonstrated in Fig. 4d and e, respectively. Both devices show photocurrent generation ability throughout the entire gate voltage range, which is also consistent with the results previously reported for monolayer  $\text{MoS}_2$  transistors.<sup>40</sup> However, the photoresponse of the  $\text{Cu}_x\text{S}@\text{MoS}_2$  device is more significant, with a negligible gate dependence, and exhibiting a linear relationship with the increase of illumination power, which is usually more desirable for practical optoelectronics.

The output curves in the dark and light states for both devices are further shown in Fig. 4f and g. It is worth mentioning that the linear relationship between the drain current and drain voltage

indicates good ohmic contact of the channel materials and contact electrodes. One can again observe that the  $\text{Cu}_x\text{S}@MoS_2$  device exhibits a more substantial photoresponse compared to the  $\text{Cu}_x\text{S}/MoS_2$  device. The output curves of the  $\text{Cu}_x\text{S}@MoS_2$  device at various illumination wavelengths are shown in Fig. 4h. The device shows remarkable response for wavelengths spanning from violet to near infrared region due to the presence of small-band gap  $\text{Cu}_x\text{S}$ , which is one of the key advantages of the heterostructure compared to  $MoS_2$  devices. The corresponding photocurrent and the calculated photoresponsivity are further displayed in Fig. 4i. The trend of photoresponsivity variation according to the incident wavelength is consistent with the absorption curve of  $\text{Cu}_x\text{S}@MoS_2$  in Fig. 3c. It is worth noting that the photoresponsivity under near infrared incident radiation is significantly pronounced compared to the absorption spectra (consistent with the near field distribution in Fig. 3i). This should be enabled by (1) the band bending and electric field present at the heterojunction interface between  $MoS_2$  and a small-band gap material and (2) possibly the strong light-matter interaction due to the LSPR effect as theoretically predicted in Fig. 3i and experimentally demonstrated in our previous report,<sup>41</sup> further suggesting the potential of our TMD heterostructures in broadband optoelectronics.

Finally, we conducted density functional theory (DFT) calculations to understand and corroborate our experimental findings and conclusions regarding the optoelectronic properties of this heterostructure. Fig. 5a shows high symmetry points in the Brillouin zone of  $\text{Cu}_x\text{S}$  (inset atomic structure) used for the calculation. The obtained electronic band structures for  $\text{Cu}_2\text{S}$  and  $\text{Cu}_{1.8}\text{S}$  are shown in Fig. 5b and c, respectively. We find that the ideal chalcocite  $\text{Cu}_2\text{S}$  has an indirect band gap of 0.56 eV, however, the band structure can be effectively modulated by introducing Cu vacancies in the system. For instance, the chalcocite  $\text{Cu}_{1.8}\text{S}$  is found to exhibit a direct band gap of 0.55 eV (Fig. 5c). This suggests the incorporation of  $\text{Cu}_x\text{S}$  can not only

supplement the low IR absorption for MoS<sub>2</sub> (Fig. 3c), but also significantly improve the photoelectronic effect since the photon-related excitation and emission in the slightly deficient Cu<sub>x</sub>S are significantly improved.

The DFT calculations also reveal the work function of the components, which allows us to predict the alignment of band structure at the interface. Fig. 5d shows the band energy diagram of the Cu<sub>2</sub>S, Cu<sub>1.8</sub>S and MoS<sub>2</sub> systems before heterojunction formation. Again, this directly indicates the modulation of the band structure of Cu<sub>x</sub>S with slight variations in the stoichiometry (see more details in Figure S3, ESI†), and accordingly we are able to predict possible charge transfer pathways following heterojunction formation. As shown in Fig. 5e and f, the Cu<sub>x</sub>S-MoS<sub>2</sub> is expected to exhibit better photocarrier separation efficiency due to the formation of a type-II band alignment (Fig. 5e), as compared with the possible type-I heterojunction formed in the Cu<sub>2</sub>S-MoS<sub>2</sub> system (Fig. 5f). Thus, combined with evidence from our optical results, we can surmise that the noteworthy optoelectronic performance of our Cu<sub>x</sub>S@MoS<sub>2</sub> phototransistor is probably attributed to a comprehensive contribution from (1) improved interfacial charge transfer originated from the clean, atomically-connected interface, (2) the formation of type-II heterojunction structure between Cu<sub>x</sub>S and MoS<sub>2</sub>, and (3) potentially enhanced light-matter interactions due to the LSPR of Cu<sub>x</sub>S.

### 3. Conclusions

In summary, we explored a new route for the geometry design and synthesis of TMD heterostructures beyond traditional lateral/vertical heterostructures. The heterojunction formation was accomplished *via* a single-step direct chemical vapor deposition of MoS<sub>2</sub> on nanocrystals of

another transition metal sulfide. The resultant product, *e.g.*,  $\text{Cu}_x\text{S}@MoS_2$  heterostructures, have an appreciable atomically-sharp interface area and are found to exhibit strongly improved light-matter interactions over a broad wavelength range. The formation of this heterojunction also leads to useful band alignment and can potentially facilitate the charge separation and transfer in an optoelectronic process. The field-effect phototransistor based on the  $\text{Cu}_x\text{S}@MoS_2$  heterostructures represents interesting transfer characteristics; and importantly, constant photoresponse is observed throughout the entire positive and negative gate voltage region. The photocurrent generation was observed over a broadband range, particularly for the near infrared photodetection enabled by the band alignment at the heterojunction as well as the surface plasmon effect from  $\text{Cu}_x\text{S}$ . As such, this geometry potentially serves as a new scalable material system for future optoelectronic semiconductor devices.

### **Acknowledgements**

This material is based upon work supported by the National Science Foundation (NSF) under Grant No. DMR-1507810. This work made use of the EPIC, Keck-II, and/or SPID facilities of Northwestern University's *NUANCE* Center, which has received support from the Soft and Hybrid Nanotechnology Experimental (SHyNE) Resource (NSF ECCS-1542205); the MRSEC program (NSF DMR-1720139) at the Materials Research Center; the International Institute for Nanotechnology (IIN); the Keck Foundation; and the State of Illinois, through the IIN. J.G.D. gratefully acknowledges support from the National Science Foundation Graduate Research Fellowship Program (NSF-GRFP). A.A.M. gratefully acknowledges support from the Ryan Fellowship and the International Institute for Nanotechnology at Northwestern University.

## References

- 1 Q. H. Wang, K. Kalantar-Zadeh, A. Kis, J. N. Coleman, and M. S. Strano, Electronics and Optoelectronics of Two-Dimensional Transition Metal Dichalcogenides. *Nat. Nanotechnol.*, 2012, **7**, 699.
- 2 M. Chhowalla, D. Jena, and H. Zhang, Two-dimensional semiconductors for transistors. *Nat. Rev. Mater.*, 2016, **1**, 16052.
- 3 C. Tan, Z. Liu, W. Huang, and H. Zhang, Non-volatile resistive memory devices based on solution-processed ultrathin two-dimensional nanomaterials. *Chem. Soc. Rev.*, 2015, **44**, 2615.
- 4 H. Zhang, Ultrathin two-dimensional nanomaterials. *ACS Nano*, 2015, **9**, 9451.
- 5 X. Zhang, Z. Lai, Q. Ma, and H. Zhang, Novel structured transition metal dichalcogenide nanosheets. *Chem. Soc. Rev.*, 2018, **47**, 3301.
- 6 C. Tan, X. Cao, X. Wu, Q. He, J. Yang, X. Zhang, J. Chen, W. Zhao, S. Han, G. H. Nam, M. Sindoro, and H. Zhang, Recent advances in ultrathin two-dimensional nanomaterials. *Chem. Rev.*, 2017, **117**, 6225.
- 7 Y. Gong, J. Lin, X. Wang, G. Shi, S. Lei, Z. Lin, and H. Terrones, Vertical and in-plane heterostructures from WS<sub>2</sub>/MoS<sub>2</sub> monolayers. *Nat. Mater.*, 2014, **13**, 1135.
- 8 C. Huang, S. Wu, A. M. Sanchez, J. J. Peters, R. Beanland, J. S. Ross, and X. Xu, Lateral heterojunctions within monolayer MoSe<sub>2</sub>-WSe<sub>2</sub> semiconductors. *Nat. Mater.*, 2014, **13**, 1096.
- 9 M. Y. Li, Y. Shi, C. C. Cheng, L. S. Lu, Y. C. Lin, H. L. Tang, and W. H. Chang, Epitaxial growth of a monolayer WSe<sub>2</sub>-MoS<sub>2</sub> lateral pn junction with an atomically sharp interface. *Science*, 2015, **349**, 524.

- 10 X. Duan, C. Wang, J. C. Shaw, R. Cheng, Y. Chen, H. Li, and J. Jiang, Lateral epitaxial growth of two-dimensional layered semiconductor heterojunctions. *Nat. Nanotechnol.*, 2014, **9**, 1024.
- 11 F. Ceballos, M. Z. Bellus, H. Y. Chiu, and H. Zhao, Ultrafast charge separation and indirect exciton formation in a MoS<sub>2</sub>-MoSe<sub>2</sub> van der Waals heterostructure. *ACS Nano*, 2014, **8**, 12717.
- 12 H. Chen, X. Wen, J. Zhang, T. Wu, Y. Gong, X. Zhang, and W. Zhuang, Ultrafast formation of interlayer hot excitons in atomically thin MoS<sub>2</sub>/WS<sub>2</sub> heterostructures. *Nat. Commun.*, 2016, **7**, 12512.
- 13 D. Kozawa, A. Carvalho, I. Verzhbitskiy, F. Giustiniano, Y. Miyauchi, S. Mouri, and G. Eda, Evidence for fast interlayer energy transfer in MoSe<sub>2</sub>/WS<sub>2</sub> heterostructures. *Nano Lett.*, 2016, **16**, 4087.
- 14 X. Sun, H. Deng, W. Zhu, Z. Yu, C. Wu, and Y. Xie, Interface Engineering in Two-Dimensional Heterostructures: Towards an Advanced Catalyst for Ullmann Couplings. *Angew. Chem. Int. Ed.*, 2016, **55**, 1704.
- 15 Y. Wen, L. Yin, P. He, Z. Wang, X. Zhang, Q. Wang, and F. Wang, Integrated high-performance infrared phototransistor arrays composed of nonlayered PbS-MoS<sub>2</sub> heterostructures with edge contacts. *Nano Lett.*, 2016, **16**, 6437.
- 16 P. Sahatiya, A. Kadu, H. Gupta, P. Thanga Gomathi, and S. Badhulika, Flexible disposable cellulose paper based MoS<sub>2</sub>-Cu<sub>2</sub>S hybrid for wireless environmental monitoring and multifunctional sensing of chemical stimuli. *ACS Appl. Mater. Interfaces.*, 2018, **10**, 9048.
- 17 J. Schornbaum, B. Winter, S. P. Schießl, F. Gannott, G. Katsukis, D. M. Guldi, and J. Zaumseil, Epitaxial Growth of PbSe Quantum Dots on MoS<sub>2</sub> Nanosheets and their Near-Infrared Photoresponse. *Adv. Func. Mater.*, 2014, **24**, 5798.



- 18 D. Kufer, I. Nikitskiy, T. Lasanta, G. Navickaite, F. H. Koppens, G. Konstantatos, Hybrid 2D-0D MoS<sub>2</sub>-PbS quantum dot photodetectors. *Adv. Mater.*, 2015, **27**, 176.
- 19 A. B. Wong, S. Brittman, Y. Yu, N. P. Dasgupta, and P. Yang, Core-shell CdS-Cu<sub>2</sub>S nanorod array solar cells. *Nano Lett.*, 2015, **15**, 4096.
- 20 A. B. Martinson, S. C. Riha, E. Thimsen, J. W. Elam, and M. J. Pellin, Structural, optical, and electronic stability of copper sulfide thin films grown by atomic layer deposition. *Energy Environ. Sci.*, 2013, **6**, 1868.
- 21 Y. Wang, H. Li, Y. Zhang, Y. Peng, P. Zhang, J. Zhao, Self-templating thermolysis synthesis of Cu<sub>2-x</sub>S@M (M= C, TiO<sub>2</sub>, MoS<sub>2</sub>) hollow spheres and their application in rechargeable lithium batteries. *Nano Res.*, 2018, 11, 831.
- 22 C. Pan, S. Niu, Y. Ding, L. Dong, R. Yu, Y. Liu, Z. L. Wang, Enhanced Cu<sub>2</sub>S/CdS coaxial nanowire solar cells by piezo-phototronic effect. *Nano Lett.*, 2012, **12**, 3302.
- 23 Y. Li, K. Burnham, J. Dykes, N. Chopra, Self-patterning of graphene-encapsulated gold nanoparticles for surface-enhanced Raman spectroscopy. *MRS Commun.*, 2018, **8**, 79.
- 24 K. M. McCreary, A. T. Hanbicki, J. T. Robinson, E. Cobas, J. C. Culbertson, A. L. Friedman, and B. T. Jonker, *Adv. Funct. Mater.*, 2014, **24**, 6449.
- 25 A. S. George, Z. Mutlu, R. Ionescu, R. J. Wu, J. S. Jeong, H. H. Bay, and C. S. Ozkan, *Adv. Funct. Mater.*, 2014, **24**, 7461.
- 26 M. C. Biesinger, B. R. Hart, R. Polack, B. A. Kobe, and R. S. C. Smart, Analysis of mineral surface chemistry in flotation separation using imaging XPS. *Miner. Eng.*, 2007, **20**, 152.
- 27 S. Wang, X. Wang, and J. H. Warner, All Chemical Vapor Deposition Growth of MoS<sub>2</sub>: h-BN Vertical Van der Waals Heterostructures. *ACS Nano*, 2015, **9**, 5246.

- 28 H. Li, Q. Zhang, C. C. R. Yap, B. K. Tay, T. H. T. Edwin, A. Olivier, and D. Baillargeat, From bulk to monolayer MoS<sub>2</sub>: evolution of Raman scattering. *Adv. Funct. Mater.*, 2012, **22**, 1385.
- 29 G. Eda, H. Yamaguchi, D. Voiry, T. Fujita, M. Chen, and M. Chhowalla, Photoluminescence from chemically exfoliated MoS<sub>2</sub>. *Nano Lett.*, 2011, **11**, 5111.
- 30 W. Choi, M. Y. Cho, A. Konar, J. H. Lee, G. B. Cha, S. C. Hong, and S. Kim, High-Detectivity Multilayer MoS<sub>2</sub> Phototransistors with Spectral Response from Ultraviolet to Infrared. *Adv. Mater.*, 2012, **24**, 5832.
- 31 Y. Li, J. D. Cain, E.D. Hanson, A.A. Murthy, S. Hao, F. Shi, Q. Li, C. Wolverton, X. Chen, V. P. Dravid, Au@ MoS<sub>2</sub> core-shell heterostructures with strong light-matter interactions. *Nano Lett.*, 2016. **16**, 7696.
- 32 W. H. Chae, J. D. Cain, E. D. Hanson, A. A. Murthy, V. P. Dravid, Substrate-induced strain and charge doping in CVD-grown monolayer MoS<sub>2</sub>. *Appl. Phys. Lett.*, 2017, **111**, 143106.
- 33 B. T. Draine, and P. J. Flatau, User guide for the discrete dipole approximation code DDSCAT 7.3. *arXiv preprint arXiv* 2013, 1305.6497.
- 34 Y. Li, W. Shi, and N. Chopra, Functionalization of multilayer carbon shell-encapsulated gold nanoparticles for surface-enhanced Raman scattering sensing and DNA immobilization. *Carbon*, 2016, **100**, 165.
- 35 A. C. Poulouse, S. Veerananarayanan, M. S. Mohamed, Y. Nagaoka, R. R. Aburto, T. Mitcham, and T. Maekawa, Multi-stimuli responsive Cu<sub>2</sub>S nanocrystals as trimodal imaging and synergistic chemo-photothermal therapy agents. *Nanoscale*, 2015, **7**, 8378.
- 36 J. M. Luther, P. K. Jain, T. Ewers, A. P. Alivisatos, Localized surface plasmon resonances arising from free carriers in doped quantum dots. *Nat. Mater.*, 2011, **10**, 361.

- 37 Y. Xie, A. Riedinger, M. Prato, A. Casu, A. Genovese, P. Guardia, S. Sottini, C. Sangregorio, K. Miszta, and S. Ghosh, Copper Sulfide Nanocrystals with Tunable Composition by Reduction of Covellite Nanocrystals with  $\text{Cu}^+$  ions. *J. Am. Chem. Soc.*, 2013, **135**, 17630.
- 38 D. Jariwala, V. K. Sangwan, C. C. Wu, P. L. Prabhumirashi, M. L. Geier, T. J. Marks, and M. C. Hersam, Gate-Tunable Carbon Nanotube-MoS<sub>2</sub> Heterojunction pn Diode. *Proc. Natl. Acad. Sci.*, 2013, **110**, 18076.
- 39 Z. Yin, H. Li, H. Li, L. Jiang, Y. Shi, Y. Sun, and H. Zhang, Single-layer MoS<sub>2</sub> phototransistors. *ACS Nano*, 2011, **6**, 74.
- 40 O. Lopez-Sanchez, D. Lembke, M. Kayci, A. Radenovic, and A. Kis, Ultrasensitive photodetectors based on monolayer MoS<sub>2</sub>. *Nat. nanotechnol.*, 2013, **8**, 497.
- 41 Y. Li, J. G. DiStefano, A. A. Murthy, J. D. Cain, E. D. Hanson, Q. Li, F. C. Castro, X. Chen, V. P. Dravid, Superior Plasmonic Photodetectors Based on Au@ MoS<sub>2</sub> Core-Shell Heterostructures. *ACS Nano*, 2017, **11**, 10321.

## Figures:

**Fig. 1. Synthesis of  $\text{Cu}_x\text{S}@/\text{MoS}_2$  heterostructures.** (a) Schematic illustrating the synthesis steps, including (1) annealing, (2) sulfurization, and (3) CVD. (b) Schematic of a single  $\text{Cu}_x\text{S}@/\text{MoS}_2$  heterostructure, illustrating the cap-like  $\text{MoS}_2$  layers encapsulating a  $\text{Cu}_x\text{S}$  nanocrystal. (c) Optical view and (d,e) SEM images of the product after CVD. The substrate was left unexposed to copper film in the dotted line region in (c). (f,g) TEM images of individual  $\text{Cu}_x\text{S}@/\text{MoS}_2$  heterostructures. (h) High-resolution TEM image indicates the atomic contact at the  $\text{Cu}_x\text{S}-\text{MoS}_2$  interface and (i) the resultant diffraction pattern. (j) STEM image of a single heterostructure and (k-m) the corresponding EDS maps.

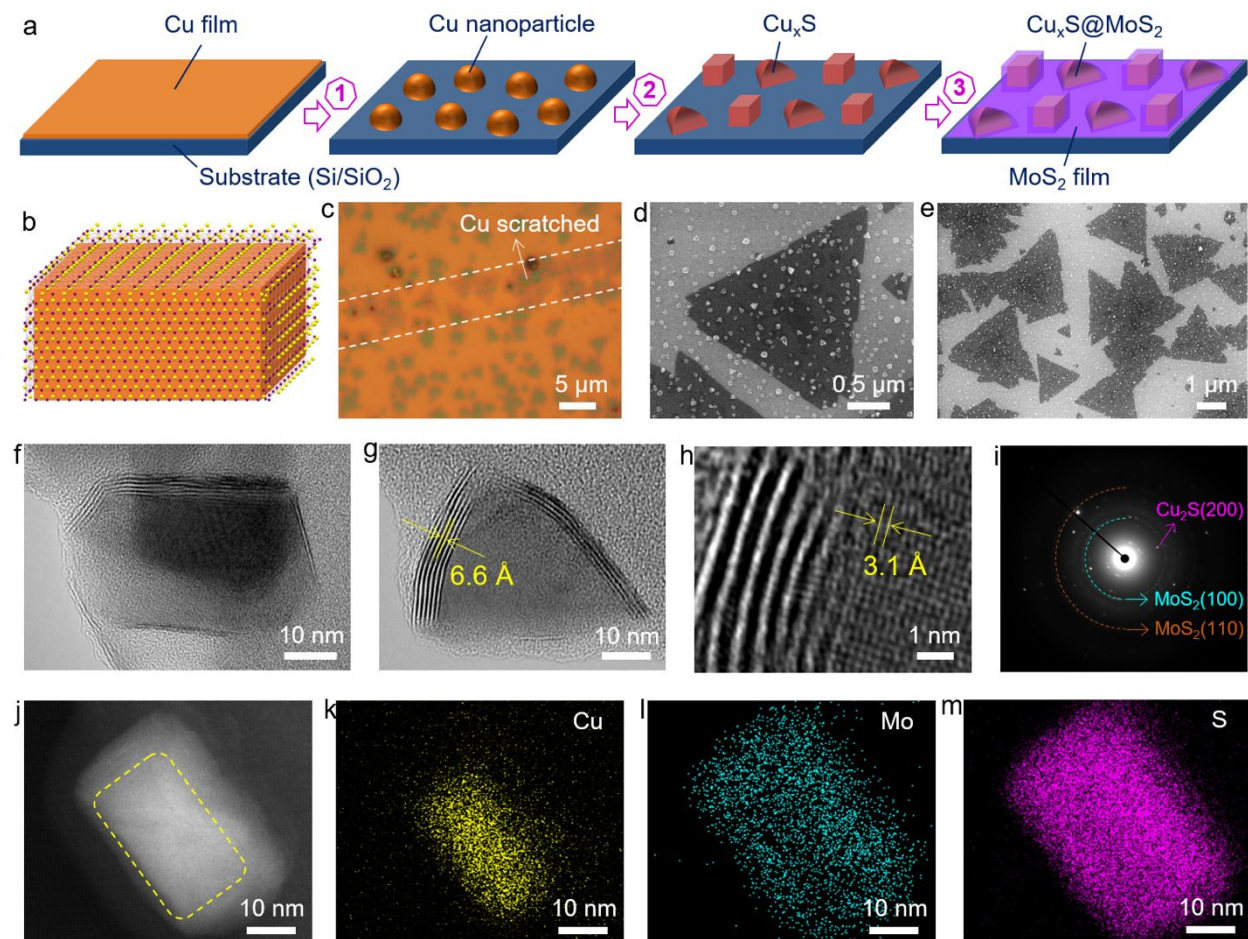


**Fig. 2. Spectroscopic characterizations.** (a-c) XPS spectra of (a) Mo 3d, (b) S 2p and (c) Cu 2p for the  $\text{Cu}_x\text{S}@/\text{MoS}_2$  heterostructures and conventional  $\text{MoS}_2$  monolayer transferred onto  $\text{Cu}_x\text{S}$  nanocrystals. (d) Raman and (e) photoluminescence spectra for (1) monolayer  $\text{MoS}_2$  inside the dotted lines in Fig. 1c, (2) conventional  $\text{MoS}_2$  monolayer transferred onto  $\text{Cu}_x\text{S}$  nanocrystals and (3)  $\text{Cu}_x\text{S}@/\text{MoS}_2$  heterostructures.

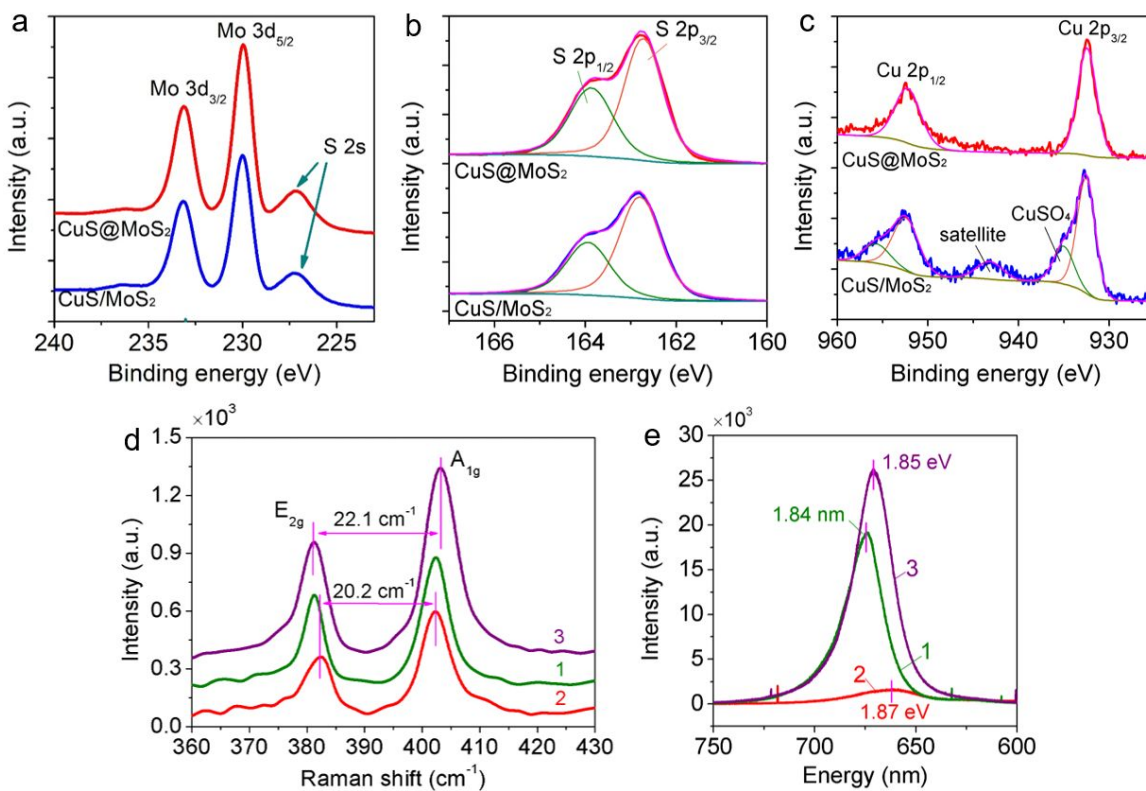


**Fig. 3. Simulation of light-matter interactions.** (a,b) 3D models for the  $\text{Cu}_x\text{S}$  (a) and  $\text{Cu}_x\text{S}@MoS_2$  (b) targets used for the DDA modeling. The arrows indicate the direction of incident light applied for all simulated targets unless otherwise noted. (c) Calculated extinction (absorption + scattering) efficiency as a function of incident wavelength. The A and B labels are corresponding to the A and B excitons observed in the photoluminescence spectra (Figure 2e). (d-i) Calculated electric field distribution on  $\text{Cu}_x\text{S}$  (d-f) and  $\text{Cu}_x\text{S}@MoS_2$  (g-i) nanocrystals under various incident wavelengths: (d, g) 400 nm, (e, h) 610 nm, (f, i) 900 nm.

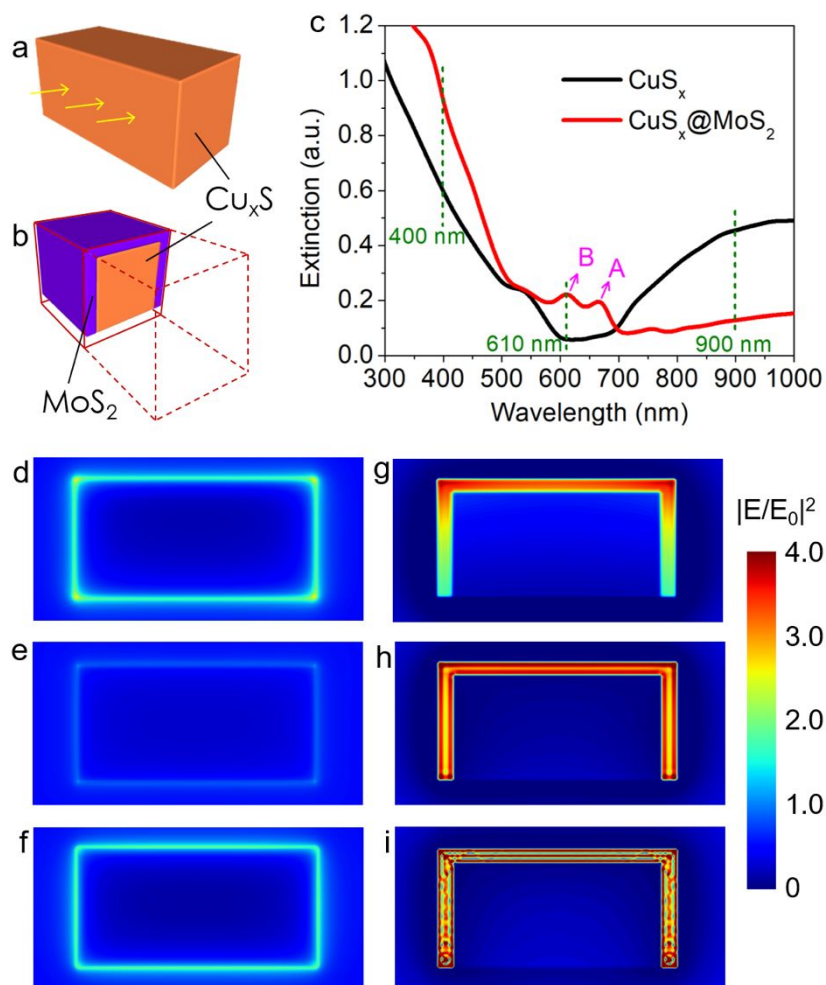




**Fig. 4. Optoelectronic device application.** (a) Device design and (b) optical view of the phototransistor. Scale bar in (b): 5  $\mu\text{m}$ . (c) Transfer characteristics of the  $\text{Cu}_x\text{S}/\text{MoS}_2$  and  $\text{Cu}_x\text{S}@/\text{MoS}_2$  devices. (d,e) Transfer curves of  $\text{Cu}_x\text{S}/\text{MoS}_2$  (d) and  $\text{Cu}_x\text{S}@/\text{MoS}_2$  (e) transistors under illumination with varying power. (f,g) Output curves of  $\text{Cu}_x\text{S}/\text{MoS}_2$  (f) and  $\text{Cu}_x\text{S}@/\text{MoS}_2$  (g) transistor with and without illumination. (h) Output curve of the  $\text{Cu}_x\text{S}@/\text{MoS}_2$  device with illuminations of different wavelength. (i) photocurrent and photoresponsivity of the  $\text{Cu}_x\text{S}@/\text{MoS}_2$  device as a function of illumination wavelength.

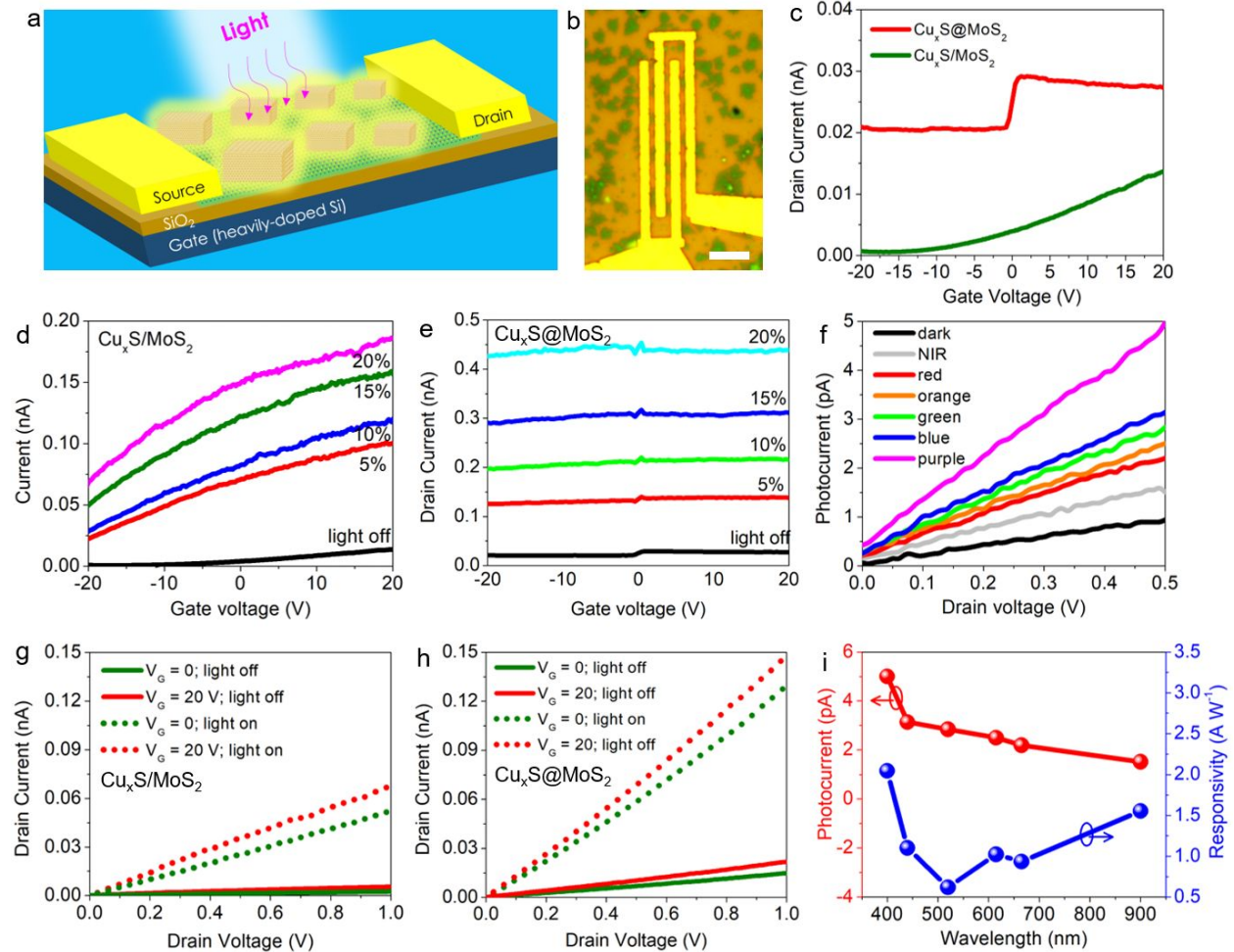


**Fig. 5. Electronic structure calculations.** (a) High symmetry points in the Brillouin zone of  $\text{Cu}_x\text{S}$ . The inset shows the corresponding atomic structure. (b,c) Band structure calculated for  $\text{Cu}_2\text{S}$  (b) and  $\text{Cu}_{1.8}\text{S}$  (c). (d) Calculated energy band diagram for  $\text{Cu}_2\text{S}$ ,  $\text{Cu}_{1.8}\text{S}$ , and  $\text{MoS}_2$ . (e,f) Schematic showing the possible formation of type-II heterojunction between  $\text{Cu}_{1.8}\text{S}$ - $\text{MoS}_2$  (e) and type-I heterojunction between  $\text{Cu}_2\text{S}$ - $\text{MoS}_2$  (f) under illumination.

